Unifying photocycle model for light adaptation and temporal evolution of cation conductance in channelrhodopsin-2

Jens Kuhne[a,1], Johannes Vierock[b,1], Stefan Alexander Tennigkeit[a], Max-Aylmer Dreier[a], Jonas Wietek[b], Dennis Petersen[a], Konstantin Gavriljuk[a], Samir F. El-Mashtoly[a], Peter Hegemann[b,2], and Klaus Gerwert[a,2]

[a]Department of Biophysics, Ruhr-Universität Bochum, 44780 Bochum, Germany; and [b]Institute of Biology, Experimental Biophysics, Humboldt-Universität zu Berlin, 10115 Berlin, Germany

Edited by F. Ulrich Hartl, Max Planck Institute of Biochemistry, Martinsried, Germany, and approved March 27, 2019 (received for review November 5, 2018)

Although channelrhodopsin (ChR) is a widely applied light-activated ion channel, important properties such as light adaptation, photocurrent inactivation, and alteration of the ion selectivity during continuous illumination are not well understood from a molecular perspective. Herein, we address these open questions using single-turnover electrophysiology, time-resolved step-scan FTIR, and Raman spectroscopy of fully dark-adapted ChR2. This yields a unifying parallel photocycle model integrating now all so far controversial discussed data. In dark-adapted ChR2, the protonated retinal Schiff base chromophore ($RSBH^+$) adopts an all-*trans*,C=N-*anti* conformation only. Upon light activation, a branching reaction into either a 13-*cis*,C=N-*anti* or a 13-*cis*,C=N-*syn* retinal conformation occurs. The *anti*-cycle features sequential H^+ and Na^+ conductance in a late M-like state and an N-like open-channel state. In contrast, the 13-*cis*,C=N-*syn* isomer represents a second closed-channel state identical to the long-lived P_{480} state, which has been previously assigned to a late intermediate in a single-photocycle model. Light excitation of P_{480} induces a parallel *syn*-photocycle with an open-channel state of small conductance and high proton selectivity. E90 becomes deprotonated in P_{480} and stays deprotonated in the C=N-*syn* cycle. Deprotonation of E90 and successive pore hydration are crucial for late proton conductance following light adaptation. Parallel *anti*- and *syn*-photocycles now explain inactivation and ion selectivity changes of ChR2 during continuous illumination, fostering the future rational design of optogenetic tools.

channelrhodopsin-2 | optogenetics | time-resolved FTIR | electrophysiology | photoisomerization

In neuroscience, light-activated proteins are utilized to modify the membrane potential and intracellular signal transduction processes of selected cells precisely and noninvasively with light (1, 2). The first and most widely used optogenetic tool is channelrhodopsin-2 (ChR2), a light-gated ion channel from the green alga *Chlamydomonas reinhardtii* (3, 4).

ChRs are structurally similar to the well-studied prototype of microbial rhodopsins, bacteriorhodopsin (BR) (5, 6). In both proteins, similar arranged clusters of protein-bound water molecules along pathways are crucial for proton conductance (7, 8). However, only a very few tiny alterations are required to switch the proton pump BR into an ion channel. In ChR2, light absorption of the retinal triggers a photocycle involving spectroscopically distinguishable intermediates as outlined in Fig. 1*A*. After blue-light excitation ($\lambda = 470$ nm) of the dark-state D_{470}, retinal isomerizes from all-*trans* to 13-*cis*, resulting in the red-shifted P_{500} intermediate that corresponds to K in BR. Proton transfer from the protonated retinal Schiff base chromophore ($RSBH^+$) to the counter-ion complex leads to P_{390} in ChR2 (M state in BR), possibly also split into an early and late P_{390} state (such as M_1 and M_2 in BR). P_{390} is succeeded by P_{520} (N in BR) after reprotonation of the RSB. Considering the time constants of channel opening observed in electrophysiological experiments, it has been suggested that both states, the late P_{390} (M_2) and P_{520} (N), contribute to ion conductance of the open channel (9–11). Finally, a long-lived nonconducting state P_{480} appears after channel closing. P_{480} is considered to be the last photocycle intermediate, and D_{470} is recovered from this species with a time constant of ∼40 s. The unbranched photocycle is reasonably well suited to describe a single-turnover transition starting from the dark-adapted protein, but fails to explain photocurrent changes during extended light application. During continuous illumination, photocurrents of ChR2 inactivate within milliseconds from a transient peak to a stationary level, and the initial peak current is recovered only after many seconds in darkness (3). Furthermore, the photocurrent decays biexponentially with two distinct time constants that differ by an order of magnitude and an amplitude ratio that depend on the preillumination time, excitation wavelength, and membrane voltage. Thus, the above-mentioned single-cycle model was extended to a parallel two-cycle model comprising two closed (C_1 and C_2) and two open (O_1 and O_2) states that are populated differently in the dark and during repetitive or continuous illumination (12, 13) (Fig. 1*B*). Photocurrent inactivation and differences in conductance were explained by a higher quantum efficiency for the transition from

Significance

Understanding the mechanisms of photoactivated biological processes facilitates the development of new molecular tools, engineered for specific optogenetic applications, allowing the control of neuronal activity with light. Here, we use a variety of experimental and theoretical techniques to examine the precise nature of the light-activated ion channel in one of the most important molecular species used in optogenetics, channelrhodopsin-2. Existing models for the photochemical and photophysical pathway after light absorption by the molecule fail to explain many aspects of its observed behavior, including the inactivation of the photocurrent under continuous illumination. We resolve this by proposing a branched photocycle explaining electrical and photochemical channel properties and establishing the structure of intermediates during channel turnover.

Author contributions: J.K., J.V., P.H., and K. Gerwert designed research; J.K., J.V., and S.A.T. performed research; M.-A.D., J.W., D.P., K. Gavriljuk, and S.F.E.-M. contributed new reagents/analytic tools; J.K., J.V., S.A.T., and S.F.E.-M. analyzed data; and J.K., J.V., S.A.T., M.-A.D., J.W., P.H., and K. Gerwert wrote the paper.

The authors declare no conflict of interest.

This article is a PNAS Direct Submission.

[1]J.K. and J.V. contributed equally to this work.

[2]To whom correspondence may be addressed. Email: hegemann@rz.hu-berlin.de or klaus.gerwert@bph.rub.de.

This article contains supporting information online at www.pnas.org/lookup/suppl/doi:10.1073/pnas.1818707116/-/DCSupplemental.

Published online April 19, 2019.

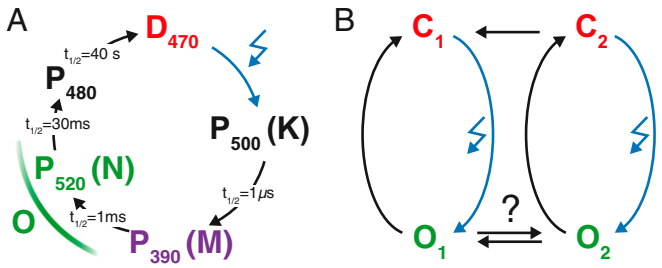

Fig. 1. Proposed photocycle models of ChR2. (*A*) Single nonbranched photocycle model starting from the IDA has been most widely used to explain time-resolved UV/VIS and FTIR experiments (9, 10, 15–18). (*B*) To explain both moderate photocurrent inactivation and slow dark-state recovery, however, a branched model with two open states is required (12, 13).

C_1 to O_1 compared with that from C_2 to O_2, consistent with recent theoretical calculations (14).

Time-resolved FTIR spectroscopy was originally established as a powerful approach for the determination of the molecular reaction mechanism of BR (19). Accordingly, the dark-adapted ChR2 photocycle was recorded between 50 ns and 140 s after exposure to a light pulse by step-scan and rapid-scan FTIR. These measurements revealed an ultrafast all-*trans* to 13-*cis* isomerization and subsequent deprotonation of the $RSBH^+$ in parallel with protonation of the counter-ion residues E123 and D253 (18). Deprotonation of D156 coincides with P_{390} depletion, which was previously considered as indicative of RSB reprotonation (17, 18). FTIR studies paired with HPLC analysis of the slow-cycling step-function variant C128T provided spectroscopic evidence for two distinct closed states with different retinal isomers (20). NMR-spectroscopic data of the ChR2 (WT) and WT-like variant H134R showed that although different closed states exist, the fully dark-adapted state [called the initial dark-adapted state (IDA)] of ChR2 is composed of 100% all-*trans*,C=N-*anti* retinal (21, 22). Raman experiments on ChR2-H134R revealed that illumination of the IDA at 80 K produced an apparent dark state (DA_{app}) containing a second retinal isomer (22). Following double isomerization around the $C_{13} = C_{14}$ and the C=N double bonds, 13-*cis*,C=N-*syn* retinal is formed, and this was proposed as the transformation step for forming the second "metastable" dark state (22). Both retinal isomers in the DA_{app} were proposed to initiate distinct photocycles, with both involving homologous P_{500}-, P_{390}-, P_{520}-, and P_{480}-like intermediates.

The central gate residue E90 is one of the key determinants of proton selectivity in ChR2 (16, 18, 23) and related cation-conducting ChRs (24). During the photocycle, E90, which is located in the central gate in the middle of the putative pore, is deprotonated and remains deprotonated until P_{480} decays (16–18). From experiments with high laser pulse repetition frequencies preventing complete dark adaptation, a late deprotonation of E90 exclusively in P_{480} was proposed for ChR2 (17). In contrast, E90 deprotonation within submicroseconds after light excitation was observed in single-turnover experiments on fully dark-adapted ChR2 (18). Thus, there seemed to be a controversy between fully dark-adapted and non–dark-adapted FTIR experiments on the timing of E90 deprotonation in a single photocycle model.

Here, we present a unifying functional study of dark- and light-adapted ChR2 by integrating single-turnover electrical recordings and FTIR measurements on ChR2, Raman spectroscopy with ^{13}C-labeled retinal, and molecular dynamics (MD) simulations. The controversies observed between single-turnover experiments and recordings under continuous illumination are resolved by developing an extended model, including two parallel photocycles with C=N-*anti* and C=N-*syn* retinal conformations. The light-adapted 13-*cis*,C=N-*syn* state is the P_{480} intermediate, which was formerly assigned to the last intermediate of the *anti*-cycle in a linear photocycle model. Within the *anti*-cycle, ion conductance evolves in two subsequent steps, resulting in two different conducting states of distinct ion selectivity ($O_{1\text{-early}}$ and $O_{1\text{-late}}$). Interestingly, E90 stays protonated in the *anti*-cycle. In contrast, the *syn*-cycle initiated by photoexcitation of P_{480}, which represents the second C_2 in Fig. 1*B*, comprises a third slowly decaying O_2 of high proton selectivity but low overall ion conductance. Conductance of O_2 depends on deprotonation of E90 and is completely abolished in the ChR2 E90Q mutant. Our results resolve the former discrepancies. In the *anti*-photocycle, E90 stays protonated and channel opening of $O_{1\text{-early}}$ and $O_{1\text{-late}}$ is observed, whereas in the *syn*-cycle, including P_{480}, E90 is deprotonated and favors proton conductance of O_2.

Results

Single-Turnover Patch-Clamp Recordings Identify Three Conducting ChR2 States. To examine functional changes during light adaptation of ChR2, we recorded single-turnover photocurrents in HEK293 cells following 7-ns laser excitation before and after light adaptation. We addressed changes in ion selectivity by reducing either the extracellular sodium (110 mM → 1 mM) or extracellular proton concentration (pH_e 7.2 → pH_e 9.0) (Fig. 2 *A* and *B*).

Under symmetrical sodium and proton concentrations, the dark-adapted ChR2 pore opens biexponentially with two almost voltage-independent time constants (150 µs and 2.5 ms). The photocurrents decline, with a dominant voltage-dependent time constant of 10–22 ms and a second, minor, slow time constant of 70–220 ms (Fig. 2 *A* and *B*, *Top*), in general agreement with previous reports (11). Decreasing extracellular Na^+ not only reduces inward-directed photocurrent amplitudes but also affects the temporal evolution of inward currents (Fig. 2*B*, *Middle*). Whereas inward currents in low extracellular Na^+ are predominantly carried by protons (H^+ flux), inward currents under symmetrical conditions are mediated by both H^+ and Na^+ ions. Subtraction of photocurrents at high and low Na^+ at pH 7.2 allows an approximation of the pure inward Na^+ flux (Fig. 2*C*). Strikingly, the proton flux peaks as early as 300 µs after excitation, significantly earlier than Na^+ flux (2.5 ms). This observation is indicative of two open states with distinct ion selectivity following single excitation of dark-adapted ChR2.

During continuous illumination, photocurrents peak within milliseconds (dependent on the light intensity) and subsequently decline to a stationary level. Inactivation is more pronounced at positive voltages, contributing to the increased inward rectification of stationary photocurrents compared with the initial peak current (3). After light adaptation, laser pulse-induced photocurrents are significantly reduced in amplitude. The photocurrent still rises and decays biexponentially, however, reaching a maximal amplitude at the same postflash time point as photocurrents in the dark-adapted protein (Fig. 2*B*). The relative photocurrent change at different time points after excitation shows a homogeneous photocurrent reduction of 60–80% between 0.2 ms and 10 ms (Fig. 2*D*). However, notably, relative photocurrent changes differ at early time points (<200 µs) and during the slow photocurrent decline (after 50–100 ms), indicating different open-state conformations in the early and late stages of the photocycle of light- and dark-adapted ChR2. In particular, at 100 ms after the laser excitation, the photocurrents even increase in amplitude for light-adapted ChR2 (especially at pH 9.0), indicative of an additional slowly decaying open state. In summary, there are at least three different conductive states: $O_{1\text{-early}}$ and $O_{1\text{-late}}$ in the dark-adapted photocycle and O_2 after light adaptation.

The proton versus sodium selectivity of all three open states is analyzed at three different time points after the actinic laser pulses (0.1 ms, 5 ms, and 100 ms; Fig. 2*E*). Although the photocurrents at 0.1 ms and 100 ms are barely distinguishable in high and low extracellular Na^+ in either the dark- or light-adapted

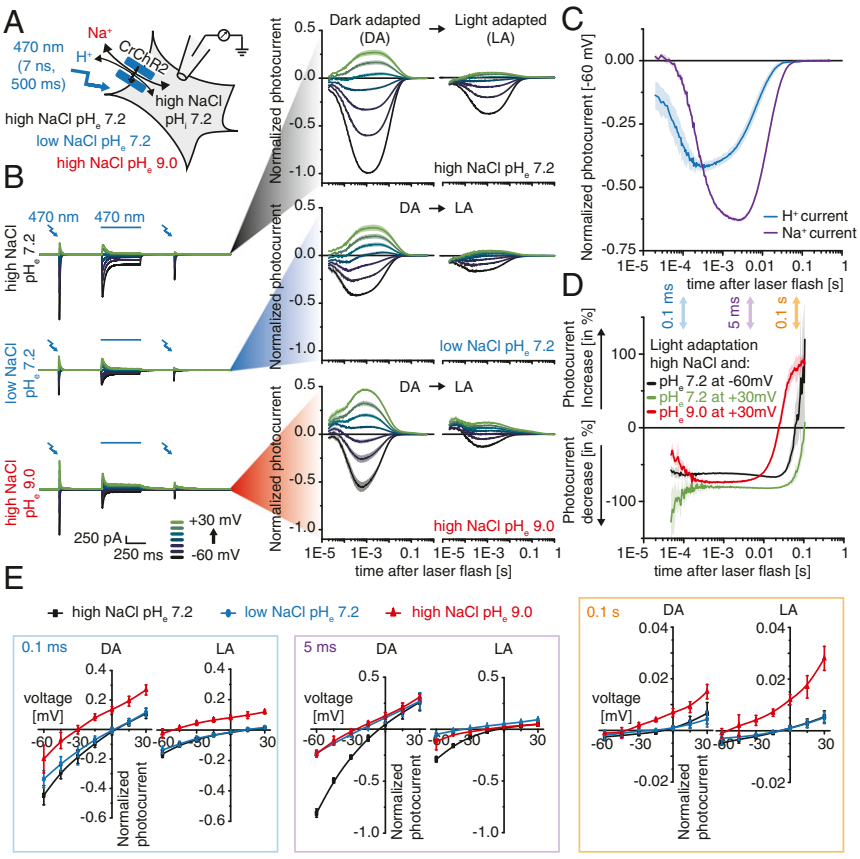

Fig. 2. Voltage-clamp recordings in HEK293 cells of photocurrents from dark- and light-adapted *ChR2* WT. (*A*) Experimental scheme of the whole-cell patch-clamp experiment in different extracellular buffers and under different illumination conditions. (*B*, *Left*) Representative photocurrents of ChR2 with intracellular 110 mM NaCl and pH_i 7.2 and extracellular 110 mM Na^+ and pH_e 7.2 (*Top*), 1 mM Na^+ and pH_e 7.2 (*Middle*), and 110 mM Na^+ and pH_e 9.0 (*Bottom*) at different holding potentials as indicated. Photocurrents were excited before and after light adaptation with a 470-nm, 7-ns laser pulse. For light adaptation, cells were continuously illuminated for 500 ms with 470-nm light. (*B*, *Right*) Normalized, log-binned, and averaged photocurrents of the dark-adapted (DA) or light-adapted (LA) protein (mean ± SEM, n = 5–8). (*C*) Time evolution of estimated proton and sodium fluxes in the DA protein at −60 mV either directly measured in extracellular 1 mM Na^+ and pH_e 7.2 (H^+ current) or calculated by subtraction of proton fluxes from combined inward flux of sodium and protons measured in symmetrical conditions (Na^+ current) (I [110 mM Na^+ (pH 7.2)] − I [1 mM Na^+ (pH 7.2)]; mean ± SEM; n = 7). (*D*) Relative photocurrent changes upon light adaptation at different extracellular voltages and pH_e [I (LA) − I (DA)]/I (DA); mean ± SEM; n = 5–8]. (*E*) Current-voltage dependency of normalized photocurrents at 0.1 ms (*Left*), 5 ms (*Center*), and 100 ms (*Right*) after excitation in different extracellular buffer compositions before (DA) and after (LA) light adaptation (mean ± SD; n = 5–8).

protein, reduction of the extracellular proton concentration causes a strong shift in reversal potential and an increase in outward-directed photocurrent amplitudes that is even more pronounced in the light-adapted channel than in the dark-adapted channel. In contrast, 5 ms after excitation of photocurrents, both ionic changes, a reduction in extracellular sodium or proton concentration, shift the reversal potential and decrease the inward photocurrent amplitude. We conclude that after channel opening, the short-lived highly proton-selective $O_{1\text{-early}}$ is followed by the more Na^+-selective but still highly proton-permeable $O_{1\text{-late}}$. After multiphoton excitation and light adaptation, the contribution of $O_{1\text{-early}}$ and $O_{1\text{-late}}$ decreases in favor of the third highly proton-selective O_2, which, although small in amplitude, significantly contributes to stationary photocurrents at alkaline pH due to its long lifetime.

Single-Turnover Time-Resolved FTIR Measurements Reveal a Splitting of the Photocycle After Light Activation of Fully Dark-Adapted ChR2. The single-turnover electrophysiology data recall that dark adaptation and light adaptation need to be compared thoroughly for the correct interpretation of time-resolved measurements. However, most time-resolved spectroscopy studies are performed with barely dark-adapted samples at rather high repetition rates to avoid long measurement times. To elucidate the underlying molecular mechanism of the observed channel-gating transitions and different ion conductance, we performed single-turnover time-resolved FTIR measurements of the fully dark-adapted ChR2 WT-like H134R variant with a time resolution of 50 ns over nine orders of magnitude (Fig. 3*A*), similar to our data from 2015 (18). The ChR2 WT-like H134R mutant shows higher protein expression in *Pichia pastoris* compared with the WT protein and has been used for the examination of light adaptation before (22). Electrical properties and photocycle kinetics are comparable, although slightly slower than those of the WT protein (25), and the same IR bands are observed in WT and in H134R. However, some crucial IR marker bands are more pronounced in H134R, which simplifies the presentation of the dataset. Dark adaptation of D_{470} was achieved by long dark periods of 140 s between pulsed excitation (temperature = 15 °C), which increased the advanced step-scan measurement time to about 4 wk (18), whereas light-adapted samples take a few hours only (17). The appearance of the marker band at 1188 cm^{-1} (not time-resolved) indicates the all-*trans* to 13-*cis*,C=N-*anti* isomerization because it represents the C_{14}-C_{15} stretching vibration of 13-*cis* retinal as originally assigned in BR by site-specific isotopic labeling (26). The decay of the 1,188 cm^{-1} marker band within a microsecond (green time trace in Fig. 3*A*) indicates the formation of the M-like P_{390} intermediate with a deprotonated RSB (18). As in other microbial rhodopsins, the subsequent rise and decay of the N-like P_{520} intermediate with a reprotonated Schiff base can be monitored by its reappearance and the decay reflects formation of the all-*trans* isomer on the time scale of a few milliseconds (19). Comparing the time course of this marker band (1,188 cm^{-1}) with the single-turnover electrical measurements, we can now assign the described conducting states $O_{1\text{-early}}$ and $O_{1\text{-late}}$ to the late part of P_{390} (M_2) and P_{520} (N), respectively, which is in line with earlier reports on the WT protein (11, 18). Due to these similarities and the abundance of spectroscopic data on BR, we decided to name the ChR2 intermediates as follows: P_{500}^{K}, P_{390a}^{M1}, P_{390b}^{M2}, and P_{520}^{N}. Global fitting of the whole dataset (solid lines, Fig. 3*A*) describes the data adequately. The apparent rate constants of H134R are similar to those of earlier reports for the dark-adapted ChR2 WT (18).

Light-Induced Splitting in 13-*cis*,C=N-*anti* and 13-*cis*,C=N-*syn* $RSBH^+$ Conformations. Interestingly, an additional retinal band at an unusual low wavenumber, 1,154 cm^{-1}, appears parallel to the 1,188-cm^{-1} 13-*cis*,C=N-*anti* marker band (not time-resolved). Because

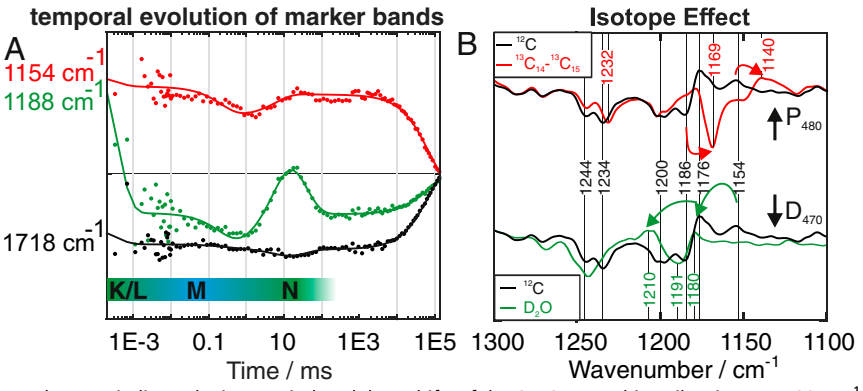

Fig. 3. FTIR measurements on H134R and WT. (*A*) Kinetic transients of the marker bands in WT-like H134R variant recorded by step-scan FTIR. The P_{480} C=N-*syn* (red) and E90 (black) marker bands, 1,154 cm^{-1} and 1,718 cm^{-1}, respectively, are observed not time-resolved at the very beginning of the reaction. Their decay occurs with the decay of P_{480} ($t_{1/2}$ = 40 s). In parallel, the $D_{470} \rightarrow P_{500}{}^{K} \rightarrow P_{390}{}^{M} \rightarrow P_{520}{}^{N}$ reaction is monitored by the marker band for protonated 13-*cis*,C=N-*anti* retinal at 1,188 cm^{-1} (green). The continuous lines are the result of a global fit analysis using five rate constants that sufficiently describe the dataset. (*B*) Comparison of unlabeled (black), $^{13}C_{14}$-$^{13}C_{15}$ labeled (red), and unlabeled but deuterated (green) WT samples in the P_{480}-D_{470} difference spectrum. The marker band at 1,188 cm^{-1} from *A* is not seen at this late photocycle intermediate. The red arrows indicate the isotope-induced downshifts of the C_{14}-C_{15} stretching vibration at 1,186 cm^{-1} in D_{470} and 1,154 cm^{-1} in P_{480}. The green arrows denote the large upshift of the C_{14}-C_{15} stretching vibration at 1,154 cm^{-1} induced by deuteration to 1,180 cm^{-1}, indicating the *syn*-conformation. Also, the C_{10}-C_{11} stretching vibration at 1,176 cm^{-1} is upshifted. The large upshift of the P_{480} bands indicates a C=N-*syn* conformation of the retinal in P_{480}. In contrast the C_{14}-C_{15} stretching vibration at 1,186 cm^{-1} in D_{470} is only slightly upshifted in D_2O to 1,191 cm^{-1}, indicating a *trans*-conformation. More details are provided in *SI Appendix, Supplementary Notes 1 and 3–5*, Figs. S1–S8, and Table S1.

the low-wavenumber band is more pronounced in H134R than in WT (*SI Appendix*, Fig. S1), we discuss the data here for the reader on the mutant, although the results are also valid for the WT. The 1,154-cm^{-1} band persists from nanoseconds to seconds after a single pulse of excitation light (Fig. 3*A*). The band is assigned here to the C_{14}-C_{15} stretching vibration of retinal because of the characteristic 14-cm^{-1} downshift upon retinal $^{13}C_{14}$-$^{13}C_{15}$ carbon-specific labeling (Fig. 3*B*, upper part). The band assignment is confirmed by additional Raman experiments (*SI Appendix*, Fig. S6). The 22-cm^{-1} upshift of the C_{14}-C_{15} band in D_2O indicates a 13-*cis*,C=N-*syn* conformation (Fig. 3*B*, lower part). In 13-*cis*,C=N-*syn* retinal, the C_{14}-C_{15} stretching vibration is strongly coupled to the N-H bending vibration, which is decoupled in D_2O (N-D) and results in a deuteration-induced large upshift in the *syn*-conformation, but not in the *anti*-conformation (27, 28). Therefore, the band at 1,154 cm^{-1} represents a 13-*cis*,C=N-*syn* marker band. The band assignments are confirmed by extended Raman experiments shown in *SI Appendix* in more detail for P_{480} (*SI Appendix, Supplementary Notes 1 and 3–5*, Figs. S1–S6, and Table S1).

The negative difference bands in Fig. 3*B* reflect vibrations of dark-adapted ChR2 WT (D_{470}). The negative band at 1,186 cm^{-1} is also assigned to the C_{14}-C_{15} stretching vibration of D_{470} because of the characteristic isotope downshift. From the additional analysis of the D_{470} Raman spectrum (*SI Appendix, Supplementary Notes 3 and 4*), we conclude that the retinal of dark-adapted ChR2 is in a 100% all-*trans*,C=N-*anti* conformation, in agreement with NMR data (21, 22). A detailed band assignment of the P_{480} and D_{470} vibrational spectra and retinal conformations is provided in *SI Appendix, Supplementary Notes 1 and 3–5*, Figs. S1–S7, and Table S1.

The parallel but temporally unresolved appearance of the bands at 1,188 cm^{-1} and 1,154 cm^{-1} in single-turnover experiments in Fig. 3*A* indicates that light absorption induces parallel isomerization of all-*trans*,C=N-*anti* retinal in D_{470} into either a 13-*cis*,C=N-*anti* or a 13-*cis*,C=N-*syn* conformation. The splitting ratio into parallel *syn*- and *anti*-pathways can be estimated as 1:1 under our measurement conditions (*SI Appendix*, Fig. S3).

Considering that the 13-*cis*,C=N-*syn* isomerization occurs in parallel to the 13-*cis*,C=N-*anti* isomerization, we conclude that the 13-*cis*,C=N-*syn* retinal conformation observed in P_{480} is therefore not the last intermediate of the 13-*cis*,C=N-*anti* photocycle, as proposed in the single-cycle model. P_{480} reflects a long-lived 13-*cis*,C=N-*syn* state, which appears in parallel to 13-*cis*,C=N-*anti* state instantaneously.

The conclusion that the P_{480} is not the last intermediate of the 13-*cis*, C=N-*anti* single photocycle but appears in parallel to the light-adapted state is furthermore strongly supported by detailed Raman experiments, as described in *SI Appendix*. The Raman results are in agreement with former Raman studies on light adaption (22). Upon complete light adaptation of ChR2 due to long illumination periods, a D_{app} state evolves. It is composed of a 40:60 mixture of the all-*trans*,C=N-*anti* species in D_{470} and the 13-*cis*,C=N-*syn* species in P_{480} (*SI Appendix*, Fig. S3). The bands observed in the Raman spectra of D_{470} and P_{480} correlate with retinal bands seen in the IR difference spectra in Fig. 3*B* and are in agreement with the published Raman spectra of the all-*trans*,C=N-*anti* and 13-*cis*,C=N-*syn* bands of the D_{app} state (22) (*SI Appendix, Supplementary Note 3*). The Raman data confirm the ultrafast C=N-*syn* formation in P_{480} as seen in Fig. 3*A* at 1,154 cm^{-1}.

E90 Deprotonates upon 13-*cis*,C=N-*syn* Formation. The E90-deprotonation marker band (1,718 cm^{-1}) (18) and the C=N-*syn* marker band (1,154 cm^{-1}) (Fig. 3*A*) appear instantaneously, and are not time-resolved. Both marker bands persist alongside the dark-adapted *anti*-cycle intermediates ($P_{500}{}^{K}$, $P_{390}{}^{M}$, and $P_{520}{}^{N}$). Both decay with a slow $t_{1/2}$ of ∼40 s. We therefore conclude that E90 remains deprotonated during the entire C=N-*syn* pathway. However, E90 does not deprotonate in the *anti*-cycle. This resolves the former discrepancies between Lórenz-Fonfría et al. (17) and Kuhne et al. (18). In agreement with the former findings, E90 deprotonates in P_{480}, but this intermediate and E90 deprotonation appear not late in the last intermediate, as proposed in a linear photocycle (17), but much faster, with the appearance of P_{480} during light adaptation in a parallel photocycle (18). In addition, E90 deprotonation appears to be closely connected to helix hydration, as indicated by the helix hydration marker bands (1,662 cm^{-1} in D_{470} and 1,650 cm^{-1} in P_{480}) that were assigned in an earlier study, but only for P_{480} (11). Interestingly, the same P_{480} hydration marker bands that are present in the WT were no longer observed in the mutants E90Q, E123T, and K93S that prevent E90 deprotonation (*SI Appendix, Supplementary Note 2* and Fig. S1). Therefore, E90 deprotonation seems to be induced by the all-*trans*,C=N-*anti* → 13-*cis*,C=N-*syn* isomerization and modulates the water influx in P_{480}.

Excitation of P_{480} Induces a Parallel Photocycle. After light adaptation, both D_{470} and P_{480} serve as parent states for parallel photocycles. At flash frequencies of 0.2 Hz that do not allow sufficient dark-state recovery, a biexponential decay with a fast process ($t_{1/2}$ = 30 ms) and a slow process ($t_{1/2}$ = 250 ms) was observed. The corresponding amplitude spectra are shown in Fig. 4*C* (also *SI Appendix, Supplementary Note 6* and Fig. S8). The 30-ms amplitude spectrum exhibits positive ultraviolet/visible (UV/VIS)

bands at 380 nm and 520 nm (Fig. 4*B*), indicative of a mixture of P_{390}^{M} and P_{520}^{N} intermediates in the C=N-*anti* cycle. In contrast, if the sample is sufficiently dark-adapted (0.005-Hz flash repetition rate), the 250-ms component is no longer observed. We therefore conclude that the slow time constant reflects the conducting state of the *syn*-cycle (Fig. 4*A*). Because the $t_{1/2}$ = 30 ms process reflects an apparent, but not an intrinsic, rate constant, the decay of both intermediates, which follows different intrinsic rate constants, is described by the integrated apparent rate.

The amplitude spectrum of the 250-ms apparent rate constant indicates decaying intermediates of the *syn*-cycle. As there is only a positive band at 520 nm, it was designated the $P^{*}_{520}{}^{N}$ intermediate to distinguish it from the P_{520}^{N} of the *anti*-cycle. The $P^{*}_{520}{}^{N}$ kinetics shown in Fig. 4 fit well to the slow photocurrent component O_2 shown in Fig. 2, and are assigned to it in the following. In contrast, no P_{390}^{M}-like intermediate is observed in the *syn*-cycle (Fig. 4*B*).

FTIR Amplitude Spectra Indicate Structural Differences of O_1 and O_2. The O_1 and O_2 FTIR amplitude spectra of the 30-ms and 250-ms apparent rates are shown in Fig. 4*C*. Both decay-associated amplitude spectra exhibit negative D_{470} marker bands (Fig. 4*C* and *SI Appendix*, Figs. S8 and S10), indicating a direct transition from the *anti*- and *syn*-photocycles into the all-*trans*,C=N-*anti* configuration of D_{470}.

The $t_{1/2}$ = 30-ms FTIR decay-associated amplitude spectrum of the C=N-*anti* cycle exhibits carbonyl bands at 1,760 cm^{-1} (+)/1,736 cm^{-1} (−) and 1,728 cm^{-1} and 1,695 cm^{-1}, which were assigned to protonation of the counter-ion D253 (18, 29) (1,728 cm^{-1}) and deprotonation of D156 (1,736 cm^{-1}). Furthermore, the helix hydration marker bands at 1,662 cm^{-1} (−)/1,650 cm^{-1} are present, which are now assigned to both $O_{1\text{-early}}$ and $O_{1\text{-late}}$. In the $t_{1/2}$ = 250-ms decay-associated amplitude spectrum, all carbonyl bands are strongly reduced, including the bands of the Schiff base proton acceptor D253 (at 1,728 cm^{-1}), as well as D156 (1,736 cm^{-1}), which has been proposed to be the RSB reprotonation donor (17). Because the Schiff base deprotonation is not observed, the corresponding counter-ion D253 protonation is not seen either. Also, reprotonation of D156 (1,736-cm^{-1} band) is no longer observed. The negative P_{480} band (1,154 cm^{-1}) in the $t_{1/2}$ = 250-ms decay-associated amplitude spectrum indicates an additional $O_2 \rightarrow P_{480}$ backreaction within the *syn*-photocycle (*SI Appendix*, *Supplementary Note 6* and Figs. S8 and S10).

Isomerization of Retinal Leads to a Rearrangement of the Central Gate. To visualize the structural changes within the protein, we performed MD simulations based on the recently published crystal structure of ChR2 WT [Protein Data Bank (PDB) ID code 6EID] (30). The structure of ChR2 is highly similar to the structure of the ChR1-like chimera C1C2; however, in contrast to the latter, in the ChR2 structural model, E90 is already "downward"-oriented in the dark-adapted state and at the same position as observed for the C1C2 chimera structural model after isomerization (18, 31). Within our simulations of the ChR2 WT structure presented here, the retinal isomerization was changed from the dark-adapted all-*trans*,C=N-*anti* conformation (Fig. 5*C*, *Left*) to either a 13-*cis*,C=N-*anti* single isomerization (*SI Appendix*, *Supplementary Note 7* and Fig. S13 *A* and *B*) or a 13-*cis*,C=N-*syn* double isomerization (Fig. 5*C*, *Right* and *SI Appendix*, Fig. S13*C*). The observed changes in hydrogen bond interaction and water distribution are shown in Fig. 5 *B* and *C* and *SI Appendix*, Figs. S12–S14. It is noteworthy that the single isomerization induces an upward orientation of the RSB proton, whereas the position of the RSB proton is only slightly changed in the double isomerization (16, 22) (Fig. 5*A*). Starting from the WT structure, E90 keeps its initial downward orientation in the dark-adapted state (Fig. 5 *B* and *C*). Very recently, a more advanced method to perform such isomerization simulations was introduced by Ardevol and Hummer (31). They simulated a homology model of ChR2 based on the C1C2 chimera crystal structure (PDB ID code 3UG9) (32) and obtained a downward flip of the initially upward-orientated E90. We have already observed the same downward movement in our model based on the same crystal structure using a classical approach (18). This proves that even our classical approach correctly predicts alterations of the hydrogen bond pattern of E90 due to retinal isomerization. It seems that E90 is trapped in a local minimum in both models but finds the correct position for ChR2 [as observed in the PDB ID code 6eid crystal structure (30)] after disturbance by isomerization.

Following 13-*cis*,C=N-*syn* double isomerization, helices 2 and 7 stay connected via E90 and D253 as long as E90 remains protonated (*SI Appendix*, Fig. S12). Deprotonation of E90 leads to an alternative contact between E90 and K93 (Fig. 5 *B* and *C* and *SI Appendix*, Fig. S12) that opens the central gate and results in an influx of water molecules into the pore (Fig. 5*C*). This water influx is in agreement with the channel opening due to E90 deprotonation proposed formerly in the E90-Helix2-tilt (EHT) model in the 13-*cis*,C=N-*anti* conformation (18). We now attribute E90 deprotonation and pore hydration to the light-adapted closed-state P_{480}. In this light-adapted state, the inner gate still remains closed and ion permeation is hindered, in agreement with the electrophysiology results (*SI Appendix*, Fig. S14). As 13-*cis*,C=N-*syn* isomerization accumulates during light adaptation, we could attribute E90 deprotonation and pore hydration to the light-adapted closed-state P_{480}.

Deprotonation of E90 Is Essential for Proton Conductance of O_2 Following Light Adaptation. As we have shown that the deprotonation of E90 is responsible for pore hydration in the light-adapted dark-state P_{480}, an important role of E90 deprotonation for channel conductance in the *syn*-cycle appeared likely from our model. Consequently, we mutated E90 to glutamine and analyzed photocurrent changes before and after light adaptation (Fig. 6*A* and *SI Appendix*, Fig. S11). In general agreement with

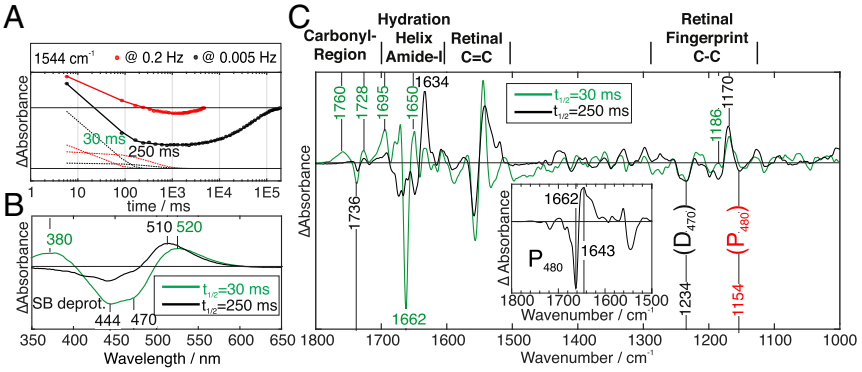

Fig. 4. Kinetic behavior of ChR2-WT at different laser pulse repetition rates. (*A*) Time-evolution of the amide-I band at 1,544 cm^{-1} at low (0.005 Hz, black) and high (0.2 Hz, red) pulse repetition frequency. Upon higher pulse repetition frequency, the decay switches from mono- to biexponential. (*B*) Comparison of O_1 (green) and O_2 (black) decay-associated UV/VIS amplitude spectra. The two positive bands at 380 nm and 520 nm in O_1 (green) indicate a mixture of P_{390}^{M2} ($O_{1\text{-early}}$) and P_{520}^{N} ($O_{1\text{-late}}$). No evidence for $RSBH^{+}$ deprotonation is visible in the slow component (O_2). (*C*) Same processes as monitored by FTIR.

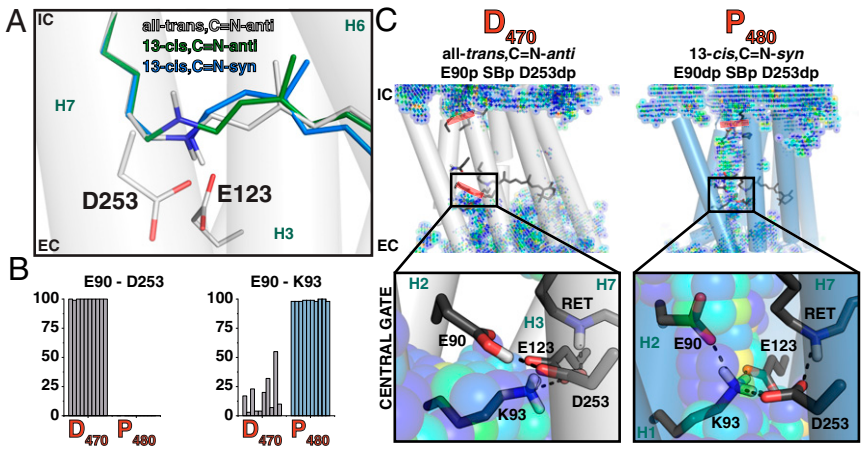

Fig. 5. Retinal conformations and formation of P_{480}. (*A*) Modeled representation of the calculated retinal configurations. The Schiff base orientations in the D_{470} structure all-*trans*,C=N-*anti* (gray) and in the modeled 13-*cis*,C=N-*anti* (green) and 13-*cis*,C=N-*syn* (blue) retinal structures are shown. (*B*) Overview of E90 hydrogen bond pattern for five independent simulations, with two monomers forming one dimer based on the ChR2 WT crystal structure [PDB ID code 6EID (30)]. Bars indicate the frequency of the respective hydrogen bond (percentage) during the 100-ns simulation. (*C*) Representative structure of the simulations is depicted. (*Left*) D_{470} dark state. (*Right*) Structure after all-*trans*,C=N-*anti* → 13-*cis*,C=N-*syn* double isomerization and E90 deprotonation (P_{480}). After deprotonation of E90, the central gate opens and water invades.

previous results of steady-state measurements (16, 33), the E90Q mutation reduces proton conductance of $O_{1\text{-late}}$ of the *anti*-cycle. Accordingly, upon reduction of extracellular sodium, photocurrent amplitudes are more decreased compared with the WT (Fig. 6*B*), and the reversal potential shifts are larger 2 ms after excitation (Fig. 6*C* and *SI Appendix*, Fig. S11*C*). In addition to the effect on the *anti*-cycle, the E90Q mutation completely abolishes the late photocurrent increase upon light adaptation, which was observed in the WT channel (*SI Appendix*, Fig. S11*D*). Instead, slow photocurrents are reduced in the E90Q mutant following continuous illumination (Fig. 6 *D* and *E*). This indicates that E90 facilitates proton conductance of O_2 by deprotonation, rendering it completely impermeable in the E90Q mutant. The results on the E90Q mutation validate our photocycle model with a parallel *syn*-cycle that involves E90 deprotonation and populates during light adaption.

Discussion

Microbial rhodopsins are excellent optogenetic tools (1–4). Understanding of their detailed mechanisms is catalyzed by earlier extended studies on BR providing detailed insight on how tiny light-induced protein alterations induce a proton transfer by an interplay of catalytic key residues and clusters of protein-bound water molecules along the proton transfer pathway (5–7). This detailed understanding paved the way for studies of several other microbial rhodopsins, like halorhodopsins, sensory rhodopsins, and especially ChRs. In the present work, we combined single laser pulses and continuous or repetitive illumination in an advanced biophysical approach to analyze the fully dark- and light-adapted ChR2 in single-turnover electrophysiological recordings, time-resolved FTIR, and resonance Raman spectroscopic measurements, complemented by MD simulations. We verified early branching into two parallel photocycles with distinct retinal isomerization and alternative configurations of the central gate, and elaborated a unifying photocycle model shown in Fig. 7 that addresses light adaptation and temporal changes in cation conductance on a functional and molecular level.

Following longer dark periods, the IDA comprises only D_{470} containing 100% all-*trans*,C=N-*anti* retinal, which is in agreement

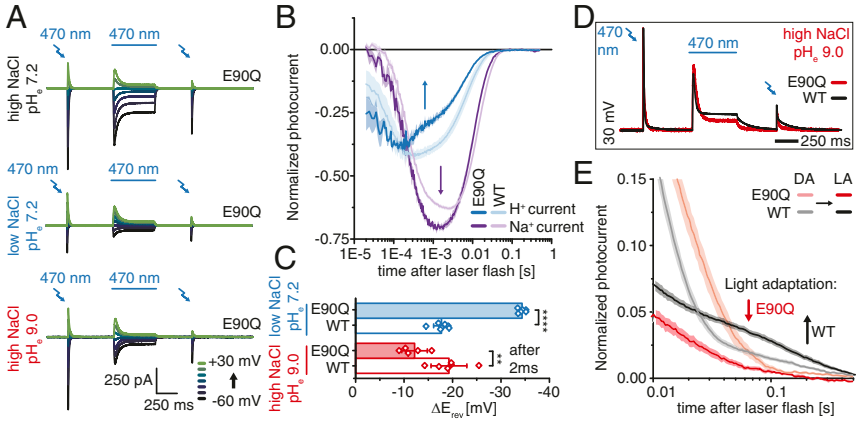

Fig. 6. Proton and sodium conductance of the dark- and light-adapted *ChR2* mutant E90Q. (*A*) Representative photocurrents of ChR2-E90Q with intracellular 110 mM NaCl and pH_i 7.2 and extracellular 110 mM Na^+ and pH_e 7.2 (*Top*), 1 mM Na^+ and pH_e 7.2 (*Middle*), 110 mM Na^+ and pH_e 9.0 (*Bottom*) at different holding voltages as indicated. Photocurrents were excited before and after light adaptation by 7-ns laser pulses of 470-nm wavelength light. For light adaptation, cells were illuminated for 500 ms with continuous 470-nm light. (*B*) Time evolution of estimated proton and sodium fluxes in the dark-adapted protein at −60 mV either directly measured in extracellular 1 mM Na^+ and pH_e 7.2 ("H^+ current") or calculated by subtraction of proton fluxes from combined inward flux of sodium and protons measured in symmetrical conditions ("Na^+ current") (*I* [110 mM Na^+ (pH 7.2)] − *I* [1 mM Na^+ (pH 7.2)]; mean ± SE; WT: $n = 7$, E90Q: $n = 6$). (*C*) Reversal potential shift (ΔE_{rev}) 2 ms after laser light excitation of the dark-adapted protein upon reduction of extracellular sodium (110 mM NaCl → 1 mM NaCl) or proton (pH_e 7.2 → pH_e 9.0) concentration (mean ± SD; E90Q: $n = 5$–6, WT: $n = 6$–7; corrected for liquid junction potentials). (*D*) Equally scaled representative photocurrents of ChR2 WT and E90Q at +30 mV and extracellular 110 mM Na^+ and pH_e 9.0. (*E*) Normalized, log-binned, and averaged photocurrents of the dark-adapted (DA) or light-adapted (LA) WT and E90Q at +30 mV and extracellular 110 mM Na^+ and pH_e 9.0 (mean ± SEM; WT: $n = 6$, E90Q: $n = 5$).

with previous reports (21, 22). The inner gate and the central gate are closed, and interhelical hydrogen bonding of D253 with the $RSBH^+$ and the protonated E90 (31) prevents the invasion of water molecules from the extracellular bulk phase. After illumination of D_{470} (C_1), early branching of the photocycle due to an alternative retinal single or double isomerization occurs.

In the classical reaction path starting from D_{470} (designated the *anti*-cycle) all-*trans*,C=N-*anti* retinal isomerizes to 13-*cis*,C=N-*anti*, leading to $P_{500}{}^{K}$, deprotonation of the $RSBH^+$ in $P_{390}{}^{M}$ and reprotonation of the RSB in $P_{520}{}^{N}$, and direct monoexponential recovery of D_{470}. Channel opening occurs at the UV/VIS silent transition from $P_{390a}{}^{M1}$ to $P_{390b}{}^{M2}$ in two subsequent steps (11) that we can now attribute to different ion selectivities pinpointing different pore conformations. Whereas during $P_{390b}{}^{M2}$, the short-lived $O_{1\text{-early}}$ conducts almost exclusively protons, photocurrents of $O_{1\text{-late}}$, which evolve upon reprotonation of the RSB and formation of $P_{520}{}^{N}$, are also carried by cations. Curiously, we observe a small positive charge displacement during $P_{520}{}^{N}$ at 0 mV and under symmetrical ionic conditions (Fig. 2) that could result from an outward-directed proton displacement following reprotonation of the RSB. This might reflect the earlier proposed residual proton transfer in ChR2 (34) that was later associated with protonation changes of D156 (17). We note that the observed small charge transfer is barely visible after light adaptation or any applied membrane potential. It occurs more than one order of magnitude later than the peak displacement current in the proton pump BR (35) and differs from fast charge transfer observed in other ChRs (36).

In the second reaction path, illumination of D_{470} (C_1) results in all-*trans*,C=N-*anti* → 13-*cis*,C=N-*syn* isomerization and direct formation of P_{480} (C_2), which is also photoreactive. Alternative photoreactions have been considered before to explain the biexponential decay of the conductive-state P_{520} (17, 37, 38), and were assumed to involve an early all-*trans*,C=N-*anti* → 13-*cis*,C=N-*syn* isomerization based on NMR and low-temperature Raman measurements (22). Using isotopically labeled retinal and vibrational spectroscopy, we proved that the early all-*trans*,C=N-*anti* → 13-*cis*,C=N-*syn* double isomerization (also at ambient temperatures) causes early formation of P_{480} (C_2). Consequently, the slowly decaying P_{480} does not represent a late photocycle intermediate of the *anti*-cycle, as proposed in several previous publications (9, 11, 17, 37), but is the result of a reaction branching that occurs directly after photoexcitation of D_{470} (C_1), possibly already during the excited-state lifetime. As shown by MD simulations, P_{480} features a preopening of the central gate, allowing water influx, but remains nonconductive because the inner gate is still closed as previously proposed for the E90R chloride-conducting mutant (23).

In a third reaction path, photoactivation of P_{480} (C_2) initiates the *syn*-cycle. Here, we identified $P^*{}_{520}{}^{N}$ as the conductive-state O_2. Under continuous illumination, $P^*{}_{520}{}^{N}$ accumulates due to its slow decay rate and significantly contributes to the stationary photocurrent, especially at high pH. Consequently, the parallel formation of $P_{520}{}^{N}$ and $P^*{}_{520}{}^{N}$ accumulation accounts for the biexponential channel-closing kinetics and the evolution of proton conductance during continuous illumination (3, 39). Comparing $P^*{}_{520}{}^{N}$ accumulation in our FTIR measurements with the small photocurrent amplitude of O_2 in our electrophysiological recordings indicates a significantly reduced conductance of O_2 ($P^*{}_{520}{}^{N}$) compared with $O_{1\text{-early}}$ ($P_{390b}{}^{M2}$) and $O_{1\text{-late}}$ ($P_{520}{}^{N}$), as previously predicted (12, 13). This now explains the ChR2 photocurrent inactivation during continuous illumination. It also explains the remarkably small shifts of the action spectra of the dark-adapted (D_{470}) and light-adapted (P_{480}) protein (40). The reduced sodium selectivity of $P^*{}_{520}{}^{N}$ (O_2) compared with $P_{520}{}^{N}$ ($O_{1\text{-late}}$) indicates substantial differences in the open-pore structures of both conducting states that are further supported by distinct FTIR spectra for $P^*{}_{520}{}^{N}$ and $P_{520}{}^{N}$. In summary, the slower decay of the *syn*-cycle with reduced conductance leads to the accumulation of P_{480} and now explains photocurrent inactivation.

Multiple dark states and different retinal isomers have been observed in other microbial rhodopsins, such as BR (41) and anabaena sensory rhodopsin (ASR) (42), before. Whereas we herein confirm photoactive all-*trans*,C=N-*anti* → 13-*cis*,C=N-*syn* as an alternative photoisomerization and an important step for light adaptation in ChRs, such a photoreaction has not been described for BR. What has been described for BR is a thermal

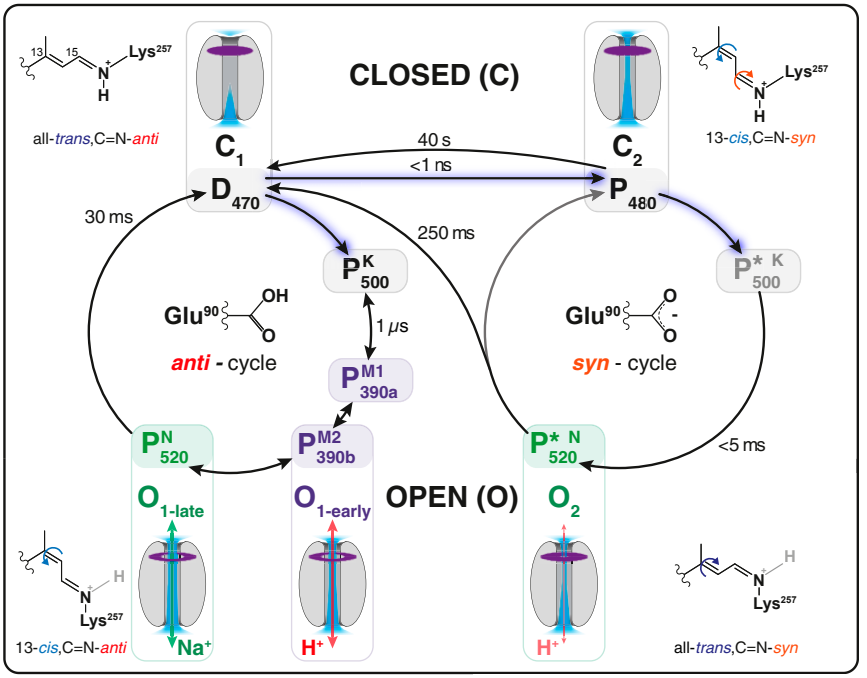

Fig. 7. Unifying photocycle model. D_{470} and P_{480} represent the closed states C_1 and C_2 of Fig. 1*B*. D_{470} is the state with all-*trans*,C=N-*anti* retinal, which is populated to almost 100% in fully dark-adapted ChR2. Upon light activation, two pathways are observed. In path 1, all-*trans*,C=N-*anti* → 13-*cis*,C=N-*anti* isomerization initiates the *anti*-photocycle, with the K-like $P_{500}{}^{K}$ that converts into M-like $P_{390}{}^{M}$ and N-like $P_{520}{}^{N}$ assigned to the open states ($O_{1\text{-early}}$) and ($O_{1\text{-late}}$). In path 2, all-*trans*,C=N-*anti* → 13-*cis*,C=N-*syn* isomerization leads to P_{480} formation with deprotonated E90. The nonconducting state P_{480} slowly relaxes back to D_{470}. At high flash frequencies or under continuous illumination, P_{480} (C_2) accumulates. The light-adapted DA_{app} represents a mixture of D_{470} and P_{480} ($C_1 + C_2$). The photoproduct of the photoreactive P_{480} (C_2) is the N-like $P^*{}_{520}{}^{N}$, which is regarded as the open state O_2. Due to its relatively long decay time $P^*{}_{520}{}^{N}$ accumulates under continuous illumination with bright light as commonly used in electrophysiology. During such conditions, both P_{480} and $P^*{}_{520}{}^{N}$ contribute to the inactivation of ChR2 as they accumulate at the expense of the highly conductive O_1 and its parent state D_{470}. E90 remains protonated during the *anti*-cycle and deprotonated during the *syn*-cycle.

equilibration between all-*trans*,C=N-*anti* (λ_{max} = 568 nm) and 13-*cis*,C=N-*syn* (λ_{max} = 548 nm) toward a ratio of roughly 6:4. Photoactivation of BR_{548} initiates the *syn*-cycle that branches either early or late to the all-*trans*,C=N-*anti* state, accumulating all molecules in the BR_{568} isoform (43, 44). The situation is different in ASR. Here, the fully dark-adapted state again contains an all-*trans*,C=N-*anti* chromophore. Photoactivation is thought to first cause a classic 13-*trans* to 13-*cis* isomerization and then a thermal obligatory C=N isomerization late during the photocycle, ending up with a 13-*cis*,C=N-*syn* light-adapted second dark state (45). Illumination of this second dark state is thought to cause 13-*cis* to *trans*-isomerization and, at the end of the *syn*-cycle, a thermal C=N *syn*- to *anti*-isomerization. In summary, in microbial rhodopsins, photochemical as well as thermal single isomerization around the $C_{13} = C_{14}$ bond and photochemical and thermal double isomerization around $C_{13} = C_{14}$ and $C_{15} = N$ are possible, but the efficiency of both reactions in light and in darkness, as well as the preferences of the directions, vary substantially within the diverse family.

Finally, we show that E90 is crucial for proton conductance in both photocycles and constitutes one key determinant for ion selectivity changes during continuous illumination with an intriguing double function depending on its protonation state before and after light adaptation. In the *anti*-cycle, E90 might be directly involved in proton transport as a proton shuttle or in the organization of water molecules, both of which bridge the distinct water-filled cavities seen in the dark-state crystal structure of ChR2 (31). In this scenario, E90 would favor proton selectivity, forming either a direct or indirect shortcut for protons that cannot be taken by larger cations at a similar efficiency. By similar means, the outer pore glutamates E139 and E143 in the highly proton-selective ChR Chrimson (46) or D112 in the voltage-gated proton channel Hv1 (47) were also shown to contribute to proton conductance and selectivity. Although the selectivity filter of ChR2, localized in the central gate, might be more permissive for larger cations than that of Chrimson, localized in the outer gate (48), in both cases, substitution of essential glutamates (E90 in ChR2 and E139 in Chrimson) by equally titratable histidines preserved proton selectivity, whereas substitution with the nontitratable glutamine or alanine impaired proton conductance (16, 46). In the *anti*-cycle, channel opening occurs with E90 staying protonated for the entire gating process. Accordingly, recent 4-μs molecular mechanics (MM) simulations on an ChR2 homology model based on the C1C2 chimera structure [PDB ID code 3ug9 (32)] showed impressively that minor hydrogen bond changes of E90 due to protonation of the counter-ion in the central gate region were sufficient to promote water invasion in the same time range (31). This water invasion weakens the electrostatic interactions of helix 2 and leads to channel opening. In our P_{390} simulations for the ChR2 WT structure (30) (*SI Appendix*, Fig. S12), we observed a similar hydrogen bond rearrangement of E90 toward E123 that allowed water influx at the longer microsecond simulation times (30). Once deprotonated in the *syn*-cycle, E90 forms a salt bridge with the adjacent K93 and completely opens the central gate (as found for C_2), promoting helix hydration from the extracellular site, as shown in our MD simulations (Fig. 5). Although the proton acceptor of E90 has not been identified yet, the close proximity to water molecules, as indicated by our MD simulations, might allow fast proton diffusion into the bulk phase. Water molecules are expected to serve as proton shuttles as they can become transiently protonated, as previously shown for BR (7). It is essential to note that pore hydration due to hydrogen bond changes of E90 in P_{390} differs from the pore hydration due to E90 deprotonation and salt bridge formation with K93 that we proposed earlier in our E90-Helix2-tilt model (18). Without considering parallel photocycles, we initially attributed early pore hydration due to E90 deprotonation to a pregating step in a linear photocycle. At the same time, early E90 deprotonation has been challenged by measurements of partly light-adapted ChR2, arguing that E90 is only deprotonated during the lifetime of P_{480}, which was assumed to be a late intermediate of a linear photocycle or a late branching reaction (11, 17, 49). Comparing FTIR measurements of dark- and light-adapted ChR2, we were able to resolve the controversy regarding E90 deprotonation. P_{480} (C_2) is formed in an ultrafast branching reaction that leads to the very fast deprotonation of E90. The splitting of the photocycle into the *anti*- and *syn*-branches forms the basis for the light adaptation of ChR2. In the E90Q mutant, all-*trans*,C=N-*anti* → 13-*cis*,C=N-*syn* isomerization still occurs but can no longer trigger deprotonation of residue E90. Consequently, in E90Q, pore hydration in the *syn*-cycle is reduced and conformational changes during formation of $P^*_{520}{}^{N}$ are no longer sufficient to support passive proton flux in the *syn*-cycle. As the *syn*-cycle is still populated in the E90Q mutant but nonconductive, photocurrents still inactivate during continuous illumination at a degree determined by the relative rate constants. As an essential revision of our previous E90-Helix2-tilt model, we therefore reassign early pore hydration to the light-dependent transition to the *syn*-cycle. Deprotonation of E90 and subsequent pore hydration prepare proton conductance of $P^*_{520}{}^{N}$ in the *syn*-cycle. However, even if E90 is not deprotonated in the *anti*-cycle, it seems still crucial for ion selectivity.

In a combined study of single-turnover electrophysiology and FTIR and Raman spectroscopy with isotopic retinal labeling, site-directed mutagenesis, and MD simulations, we developed a unifying two-photocycle model that simplifies and embraces previous kinetic models and completely resolves the channel gating, light adaptation, and temporal changes in ion selectivity. Identifying the corresponding molecular transitions, we may facilitate future protein engineering of ChR variants with reduced or improved photocurrent inactivation for optogenetic applications, requiring either a stable response to continuous illumination or a transient response to light switching. Early photocycle branching by alternative retinal isomerization and the corresponding large conformational protein changes that do not directly lead to channel opening will need careful consideration for the interpretation of molecular gating transitions observed in time-resolved spectroscopy, crystallography, and optogenetic experiments.

It turns out that only tiny light-induced alterations are crucial for the specific protein function. The elucidation of the molecular reaction mechanisms of proteins therefore deserves vibrational spectroscopic techniques like time-resolved FTIR with nanoscale spatiotemporal resolution.

Materials and Methods

Yeast Culture. *P. pastoris* strain SMD1163 cells (kindly gifted by C. Bamann, Max Planck Institute of Biophysics, Frankfurt) containing the pPIC9KChR2His10 construct were precultured in buffered glycerol complex (BMGY) medium (50). Expression of ChR2 was induced in buffered methanol complex (BMMY) medium containing 2.5 μM all-*trans* retinal (either ^{12}C, $^{13}C_{14}$,$^{13}C_{15}$-labeled or $^{13}C_{10}$,$^{13}C_{11}$-labeled) and 0.00004% biotin at an initial OD_{600} of 1 and at 30 °C and 120 rpm. Cells were harvested at an OD_{600} of 20 by centrifugation.

Membrane Preparation and Protein Purification. Cells were disrupted using a BeadBeater (Biospec Products), and membranes were isolated by ultracentrifugation. Homogenized membranes were solubilized with 1% decylmaltoside overnight. ChR2 purification was done by nickel-nitrilotriacetic acid affinity chromatography and subsequent gel filtration using a HiLoad 16/600 Superdex 200-pg column (General Electric).

Reconstitution of ChR2 into DPPC or EggPC. The purified ChR2 was reconstituted into DPPC (Avanti Polar Lipids) or EggPC (Avanti Polar Lipids). The lipids were solubilized with 2% cholate in 20 mM Hepes (pH 7.5), 100 mM NaCl, and 1 mM $MgCl_2$ by incubation at 50 °C for 10 min. Solubilized lipids and purified ChR2 were mixed at a 2:1 ratio [lipid/protein (wt/wt)] and incubated for 20 min. Detergent was removed overnight either by adsorption on Bio-Beads SM 2 (BioRad) or by dialysis.

The resulting suspension containing proteoliposomes and buffer was ultracentrifuged at 200,000 × *g* for 2 h, and the pellet was then transferred and squeezed between two CaF_2 slides to obtain an optical path length between 5 μm and 10 μm. This sample was then placed in a vacuum-tight cuvette.

Preparation of HEK Cells. Electrophysiological recordings were performed on stably expressing the ChR2-mVenus fusion construct HEK cell line (34), as previously described in detail (51). Briefly, HEK cells were cultured at 5% CO_2 and 37 °C in DMEM supplemented with 10% FBS, 100 μg/mL penicillin/streptomycin (Biochrom), 200 μg/mL zeocin, and 50 μg/mL blasticidin (Thermo Fisher Scientific). Cells were seeded onto polylysine-coated glass coverslips at a concentration of 1×10^5 cells per milliliter and supplemented with a final concentration of 1 μM all-*trans* retinal (Sigma–Aldrich). Induction of ChR2-mVenus expression was induced by addition of 0.1 μM tetracycline (Thermo Fisher Scientific).

Patch-Clamp Experiments in HEK293 Cells. Patch pipettes were pulled using a P1000 micropipette puller (Sutter Instruments) and fire-polished. Pipette resistance was 1.5–2.5 MΩ. A 140 mM NaCl agar bridge served as a reference (bath) electrode. In whole-cell recordings, membrane resistance was typically >1 GΩ, while access resistance was below 10 MΩ. Pipette capacity, series resistance, and cell capacity compensation were applied. All experiments were carried out at 23 °C. Signals were amplified (AxoPatch200B), digitized (DigiData1400), and acquired using Clampex 10.4 software (all from Molecular Devices). Holding potentials were varied in 15-mV steps between −60 and +30 mV. Extracellular buffer exchange was performed manually by adding at least 5 mL of the respective buffer to the recording chamber (500-μL chamber volume), while a Ringer Bath Handler MPCU (Lorenz Messgerätebau) maintained a constant bath level. Standard bath solutions contained 110 mM NaCl, 1 mM KCl, 1 mM CsCl, 2 mM $CaCl_2$, 2 mM $MgCl_2$, and 10 mM Hepes at extracellular pH (pH_e) 7.2 (with glucose added up to 310 mOsm). Standard pipette solutions contained 110 mM NaCl, 1 mM KCl, 1 mM CsCl, 2 mM $CaCl_2$, 2 mM $MgCl_2$, 10 mM EGTA, and 10 mM Hepes at pH_i 7.2 or 10 mM Tris at intracellular pH (pH_i) 9.0 (glucose was added up to 290 mOsm). For ion selectivity measurements, either NaCl was replaced by 110 mM *N*-methyl-D-glucamine or extracellular pH was adjusted to pH_e 9.0 by buffering with 10 mM Tris instead of Hepes.

Continuous light was generated using a Polychrome V light source (TILL Photonics) set to 470 ± 7 nm. Light exposure was controlled with a programmable shutter system (VS25 and VCM-D1; Vincent Associates). The Polychrome V light intensity was 3.4 mW/mm^2 in the sample plane, measured with a calibrated optometer (P9710; Gigahertz Optik). Light intensities were calculated for the illuminated field of the W Plan-Apochromat 40×/1.0 differential interference contrast objective (0.066 mm^2; Carl Zeiss). For delivery of 470-nm·ns^{-1} laser pulses, an Opolette polette HENd:YAG laser/OPO system (OPOTEK) was coupled/decoupled into a M37L02 multimode fiber patch cable with a modified KT110/M free space-to-fiber coupler using AC127 019 A ML achromatic doublets (Thorlabs). Single pulses were selected using a LS6ZM2 shutter (Vincent Associates). Laser intensity was set to 5% using the built-in motorized variable attenuator, resulting in a pulse energy of 100 ± 20 μJ/mm^2. Pulse energies were measured with a calibrated S470C thermal power sensor and a PM100D power and energy meter (Thorlabs) after passing through all of the optics. Actinic light was coupled into an Axiovert 100 microscope (Carl Zeiss) and delivered to the sample using a 90/10 beamsplitter (Chroma). To toggle between activation with the laser and the Polychrome V light source, a BB1 E02 broadband dielectric mirror mounted on an MFF101/M motorized filter flip mount (Thorlabs) was used. Data were filtered at 100 kHz and sampled at 250 kHz. Due to minimal timing uncertainties, each acquired sweep was time-shifted after measurements to align it with the rising edges of the Q-switch signals of the activating laser pulses. Photocurrents were binned to 50 logarithmically spaced data points per temporal decade with custom-written MATLAB script (MathWorks).

FTIR Experiments. To gain insight into the changes upon illumination, we performed time-resolved FTIR difference spectroscopy at 15 °C. For the continuous light experiments, the sample was illuminated with a blue LED (λ_{max} = 465 nm) for 5 s. Spectra were recorded before switching on the light (reference), during illumination [accumulation of the stationary photoproduct (P_{Stat}) for 5 s] and after switching off the light (decay of P_{Stat} for 500 s) using the conventional rapid scan mode of the spectrometer. Difference spectra were calculated using the Beer–Lambert law, which results in positive photo product bands and negative educt bands in the difference spectra. For the single-turnover measurements, the sample was illuminated with a short laser pulse of an excimer laser-driven dye laser (Coumarin 102 dye; λ_{max} = 475 nm, pulse width ∼ 50 ns). Conventional rapid scan experiments (time resolution ∼ 10 ms, spectral resolution = 4 cm^{-1}) were performed with a sufficient relaxation time (t_{relax} = 200 s) and flash frequency (f_{flash} = 0.005 Hz) between the flashes to allow the D_{470} to significantly repopulate ([D_{470}] became ∼96%).

For a comparison with the photocycle under the "shortcut condition," the flash frequency was increased (t_{relax} = 5 s, f_{flash} = 0.2 Hz). Using this approach, equilibrium between D_{470} and P_{480} emerges and the ChR2 molecules start the photocycle from both states. The datasets were then analyzed by a global-fitting routine as presented previously (16, 18, 52, 53) to isolate the decay-associated amplitude spectra of the transitions involved in D_{470} recovery. To get access to the earlier intermediates of the dark-adapted ([D_{470}] ∼ 91%) photocycle of H134R (Fig. 3*A*), step-scan measurements were performed with a light pulse repetition rate of 0.007 Hz (t_{relax} = 140-s, detector rise time = 50 ns, resolution = 8 cm^{-1}, wavenumber range: 0–1974 cm^{-1}) as already published for the WT (18). One measurement was completed after 22 h, and ∼15 measurements were averaged to give the final result. H134R used for the step scan was expressed in COS (abbreviation for CV-1 in Origin with SV40 genes) cells and prepared as described in our earlier publication (18).

Raman Experiments. The Raman experiments were performed with samples that were prepared exactly the same as those for the rapid scan FTIR experiments, but with a higher optical path length (20–50 μm). The room temperature was ∼18 °C. We used the Raman microscope XPloRA One (HORIBA Scientific) to scan the sample. To prevent sample degradation due to long illumination, we performed measurements at a 785-nm excitation wavelength to ensure the lowest possible photoexcitation of the sample and a sufficient enhancement of the Raman signal due to the preresonant Raman effect. Laser power at the sample position was 28 mW. A 50× objective (Olympus LCPLN-IR) was used, resulting in a confocal volume of ∼1 μm^3 in the sample plane.

To excite the D_{470} state of the sample and create a photoproduct with a high P_{480} fraction, the sample was illuminated with an external blue-light source (100-W halogen lamp filtered with a 470-nm filter coupled to the observation beam path of the microscope). Sample illumination was controlled by a shutter between the lamp and sample.

To ensure that the measured photoproduct spectra are free of contamination by their preceding intermediates (P_{520}^N and P_{390}^M) under continuous illumination, a controlled illumination/relaxation experiment was performed:

Laser on + illumination on (formation of P_{Stat})

Wait 0.5 s

Acquisition of spectrum ($t_{integration}$ = 2 s); P_{Stat} is measured

Laser on + illumination off (slow relaxation of P_{Stat}: $t_{1/2}$ ∼ 40 s)

Wait 0.5 s

Acquisition of spectrum ($t_{integration}$ = 2 s); high fraction of P_{480} free of illumination artifacts is measured (P'_{Stat})

Go to next position on the sample

This procedure was repeated for a 15 × 15 spot matrix (pixel spacing = 5 μm) of the sample, and the acquired spectra were averaged for each illumination condition.

Next, the illumination was stopped and a relaxation phase of at least 5 min was commenced to allow full relaxation of the generated P_{480}. The dark-state D_{470} was measured for the same spot matrix ($t_{integration}$ = 2 s).

To obtain the pure lamp artifact, the same area was measured without the laser with only illumination of the sample. This spectrum was later subtracted from the spectra measured under continuous illumination.

The complete protocol was performed for three spectral regions (center wavenumbers: 900 cm^{-1}, 1,250 cm^{-1}, and 1,550 cm^{-1}), which were then combined to obtain the complete spectrum ranging from 650 cm^{-1} to 1,700 cm^{-1} with a wavenumber spacing of ∼0.2 cm^{-1} and a nominal resolution of 0.6 cm^{-1}.

MD Simulations. The MD simulations were performed according to our previous reports (16, 18), except for the force field and the GROMACS version used. We used the Optimized Potentials for Liquid Simulations/All-Atom (OPLS/AA) force field and GROMACS version 2016.3. A series of 5 × 100-ns independent and unrestrained MD simulations was performed for each protonation state of E90 with the respective chromophore configuration. The MD simulations were performed consecutively using the resulting structures of dark-adapted ChR2 (all-*trans*,C=N-*anti* with protonated E90)

given by MD simulations as a starting point for the isomerization (discussed below). Each MD simulation was initiated using a different temperature seed number to generate the random distribution of starting velocities.

Water Dynamic and Run-Average Structure. The water dynamic and run-average structures were calculated according to our previous report (18).

Retinal Isomerization. Retinal all-*trans*,C=N-*anti* to 13-*cis*,C=N-*anti* isomerization was performed as described earlier (18), achieved via the following scheme. The torsion angles of the C_{13} = C_{14} and C=N double bonds were tilted counterclockwise in 20° steps, starting in the range 0–180°. For each tilting step, the retinal + K257 (without backbone) atoms were maintained as a freeze group and the rest of the simulation system was allowed to relax in a 10-ns unrestrained MD simulation as described above.

The resulting 13-*cis* retinal structures served as starting structures for the MD simulations of the different intermediates (P_{500}^{K}, P_{480}, and P_{480}-E90p) with protonated and deprotonated E90. For the starting structures for the P_{390a}^{M1} intermediate, we used the final structures of the P_{500}^{K} simulations after Schiff base deprotonation and D253 protonation.

ACKNOWLEDGMENTS. We thank Harald Chrongiewski and Gabi Smuda for technical assistance. We also thank Mathias Lübben and Till Rudack for helpful discussions. We thank Maila Reh, Altina Klein, and Tharsana Tharmalingam for technical assistance. We also thank Christiane Grimm, Joel Kaufmann, and Franz Bartl for fruitful discussions. This work was supported by the Deutsche Forschungsgemeinschaft (DFG) Priority Programme SPP 1926 and by DFG Grant SFB1078 (B2) and the Cluster of Excellence Unifying Concepts in Catalysis Berlin International Graduate School of natural Science and Engineering (BIG-NSE) (to J.V.) and E4 (to P.H.). P.H. is a Senior Research Professor of the Hertie Foundation. The spectroscopic and molecular dynamic part of this work was first presented at the 17th International Conference on Retinal Proteins in September 2016 in Potsdam, Germany. The electrophysiological work was presented for the first time at the 18th International Conference on Retinal Proteins in September 2018 in Ontario, Canada. This work was prepublished on the preprint server bioRxiv in December 2018.

1. Zhang F, et al. (2011) The microbial opsin family of optogenetic tools. *Cell* 147: 1446–1457.
2. Scheib U, et al. (2015) The rhodopsin-guanylyl cyclase of the aquatic fungus Blastocladiella emersonii enables fast optical control of cGMP signaling. *Sci Signal* 8:rs8.
3. Nagel G, et al. (2003) Channelrhodopsin-2, a directly light-gated cation-selective membrane channel. *Proc Natl Acad Sci USA* 100:13940–13945.
4. Boyden ES, Zhang F, Bamberg E, Nagel G, Deisseroth K (2005) Millisecond-timescale, genetically targeted optical control of neural activity. *Nat Neurosci* 8:1263–1268.
5. Gerwert K, Hess B, Soppa J, Oesterhelt D (1989) Role of aspartate-96 in proton translocation by bacteriorhodopsin. *Proc Natl Acad Sci USA* 86:4943–4947.
6. Lanyi JK (1992) Proton transfer and energy coupling in the bacteriorhodopsin photocycle. *J Bioenerg Biomembr* 24:169–179.
7. Garczarek F, Gerwert K (2006) Functional waters in intraprotein proton transfer monitored by FTIR difference spectroscopy. *Nature* 439:109–112.
8. Gerwert K (2017) Channelrhodopsin reveals its dark secrets. *Science* 358:1000–1001.
9. Ritter E, Stehfest K, Berndt A, Hegemann P, Bartl FJ (2008) Monitoring light-induced structural changes of Channelrhodopsin-2 by UV-visible and Fourier transform infrared spectroscopy. *J Biol Chem* 283:35033–35041.
10. Bamann C, Kirsch T, Nagel G, Bamberg E (2008) Spectral characteristics of the photocycle of channelrhodopsin-2 and its implication for channel function. *J Mol Biol* 375: 686–694.
11. Lórenz-Fonfría VA, et al. (2015) Temporal evolution of helix hydration in a light-gated ion channel correlates with ion conductance. *Proc Natl Acad Sci USA* 112:E5796–E5804.
12. Hegemann P, Ehlenbeck S, Gradmann D (2005) Multiple photocycles of channelrhodopsin. *Biophys J* 89:3911–3918.
13. Nikolic K, et al. (2009) Photocycles of channelrhodopsin-2. *Photochem Photobiol* 85: 400–411.
14. Valentini A, et al. (2017) Optomechanical control of quantum yield in trans-cis ultrafast photoisomerization of a retinal chromophore model. *Angew Chem Int Ed Engl* 56:3842–3846.
15. Verhoefen M-K, et al. (2010) The photocycle of channelrhodopsin-2: Ultrafast reaction dynamics and subsequent reaction steps. *ChemPhysChem* 11:3113–3122.
16. Eisenhauer K, et al. (2012) In channelrhodopsin-2 Glu-90 is crucial for ion selectivity and is deprotonated during the photocycle. *J Biol Chem* 287:6904–6911.
17. Lórenz-Fonfría VA, et al. (2013) Transient protonation changes in channelrhodopsin-2 and their relevance to channel gating. *Proc Natl Acad Sci USA* 110:E1273–E1281.
18. Kuhne J, et al. (2015) Early formation of the ion-conducting pore in channelrhodopsin-2. *Angew Chem Int Ed Engl* 54:4953–4957.
19. Gerwert K, Freier E, Wolf S (2014) The role of protein-bound water molecules in microbial rhodopsins. *Biochim Biophys Acta* 1837:606–613.
20. Ritter E, Piwowarski P, Hegemann P, Bartl FJ (2013) Light-dark adaptation of channelrhodopsin C128T mutant. *J Biol Chem* 288:10451–10458.
21. Becker-Baldus J, et al. (2015) Enlightening the photoactive site of channelrhodopsin-2 by DNP-enhanced solid-state NMR spectroscopy. *Proc Natl Acad Sci USA* 112: 9896–9901.
22. Bruun S, et al. (2015) Light-dark adaptation of channelrhodopsin involves photoconversion between the all-*trans* and 13-*cis* retinal isomers. *Biochemistry* 54: 5389–5400.
23. Wietek J, et al. (2014) Conversion of channelrhodopsin into a light-gated chloride channel. *Science* 344:409–412.
24. Kaufmann JCD, et al. (2017) Proton transfer reactions in the red light-activatable channelrhodopsin variant ReaChR and their relevance for its function. *J Biol Chem* 292:14205–14216.
25. Berndt A, et al. (2011) High-efficiency channelrhodopsins for fast neuronal stimulation at low light levels. *Proc Natl Acad Sci USA* 108:7595–7600.
26. Gerwert K, Siebert F (1986) Evidence for light-induced 13-cis, 14-s-cis isomerization in bacteriorhodopsin obtained by FTIR difference spectroscopy using isotopically labelled retinals. *EMBO J* 5:805–811.
27. Smith SO, et al. (1984) Determination of retinal Schiff base configuration in bacteriorhodopsin. *Proc Natl Acad Sci USA* 81:2055–2059.
28. Babitzki G, Mathias G, Tavan P (2009) The infrared spectra of the retinal chromophore in bacteriorhodopsin calculated by a DFT/MM approach. *J Phys Chem B* 113: 10496–10508.
29. Lórenz-Fonfría VA, Muders V, Schlesinger R, Heberle J (2014) Changes in the hydrogen-bonding strength of internal water molecules and cysteine residues in the conductive state of channelrhodopsin-1. *J Chem Phys* 141:22D507.
30. Volkov O, et al. (2017) Structural insights into ion conduction by channelrhodopsin 2. *Science* 358:eaan8862.
31. Ardevol A, Hummer G (2018) Retinal isomerization and water-pore formation in channelrhodopsin-2. *Proc Natl Acad Sci USA* 115:3557–3562.
32. Kato HE, et al. (2012) Crystal structure of the channelrhodopsin light-gated cation channel. *Nature* 482:369–374.
33. Ruffert K, et al. (2011) Glutamate residue 90 in the predicted transmembrane domain 2 is crucial for cation flux through channelrhodopsin 2. *Biochem Biophys Res Commun* 410:737–743.
34. Feldbauer K, et al. (2009) Channelrhodopsin-2 is a leaky proton pump. *Proc Natl Acad Sci USA* 106:12317–12322.
35. Keszthelyi L, Ormos P (2001) Electric signals associated with the photocycle of bacteriorhodopsin. *FEBS Lett* 109:189–193.
36. Sineshchekov OA, Govorunova EG, Wang J, Li H, Spudich JL (2013) Intramolecular proton transfer in channelrhodopsins. *Biophys J* 104:807–817.
37. Bamann C, Gueta R, Kleinlogel S, Nagel G, Bamberg E (2010) Structural guidance of the photocycle of channelrhodopsin-2 by an interhelical hydrogen bond. *Biochemistry* 49:267–278.
38. Stehfest K, Hegemann P (2010) Evolution of the channelrhodopsin photocycle model. *ChemPhysChem* 11:1120–1126.
39. Berndt A, Prigge M, Gradmann D, Hegemann P (2010) Two open states with progressive proton selectivities in the branched channelrhodopsin-2 photocycle. *Biophys J* 98:753–761.
40. Lin JY, Lin MZ, Steinbach P, Tsien RY (2009) Characterization of engineered channelrhodopsin variants with improved properties and kinetics. *Biophys J* 96:1803–1814.
41. Sperling W, Carl P, Rafferty Ch, Dencher NA (1977) Photochemistry and dark equilibrium of retinal isomers and bacteriorhodopsin isomers. *Biophys Struct Mech* 3: 79–94.
42. Sineshchekov OA, Spudich EN, Trivedi VD, Spudich JL (2006) Role of the cytoplasmic domain in Anabaena sensory rhodopsin photocycling: Vectoriality of Schiff base deprotonation. *Biophys J* 91:4519–4527.
43. Bryl K, Taui M, Yoshizawa M, Kobayashi T (1992) Light adaptation of dark-adapted bacteriorhodopsin studied by nanosecond time-resolved absorption spectroscopy. *Photochem Photobiol* 56:1013–1018.
44. Hofrichter J, Henry ER, Lozier RH (1989) Photocycles of bacteriorhodopsin in light- and dark-adapted purple membrane studied by time-resolved absorption spectroscopy. *Biophys J* 56:693–706.
45. Kawanabe A, Furutani Y, Jung K-H, Kandori H (2007) Photochromism of Anabaena sensory rhodopsin. *J Am Chem Soc* 129:8644–8649.
46. Vierock J, Grimm C, Nitzan N, Hegemann P (2017) Molecular determinants of proton selectivity and gating in the red-light activated channelrhodopsin Chrimson. *Sci Rep* 7: 9928.
47. Dudev T, et al. (2015) Selectivity mechanism of the voltage-gated proton channel, H_V1. *Sci Rep* 5:10320.
48. Oda K, et al. (2018) Crystal structure of the red light-activated channelrhodopsin Chrimson. *Nat Commun* 9:3949.
49. Saita M, et al. (2018) Photoexcitation of the P_4^{480} state induces a secondary photocycle that potentially desensitizes channelrhodopsin-2. *J Am Chem Soc* 140: 9899–9903.
50. Radu I, et al. (2009) Conformational changes of channelrhodopsin-2. *J Am Chem Soc* 131:7313–7319.
51. Grimm C, Vierock J, Hegemann P, Wietek J (2017) Whole-cell patch-clamp recordings for electrophysiological determination of ion selectivity in channelrhodopsins. *J Vis Exp,* e55497.
52. Müller K-H, Plesser T (1991) Variance reduction by simultaneous multi-exponential analysis of data sets from different experiments. *Eur Biophys J* 19:231–240.
53. Hessling B, Souvignier G, Gerwert K (1993) A model-independent approach to assigning bacteriorhodopsin's intramolecular reactions to photocycle intermediates. *Biophys J* 65:1929–1941.